Surfaces and Interfaces 86 (2026) 108793

Contents lists available at ScienceDirect

Surfaces and Interfaces

journal homepage: www.sciencedirect.com/journal/surfaces-and-interfaces

Effect of surface-modified nanoparticles on microstructure and hardness of low-temperature solder alloys

Shunya Nitta [a,b,*], Hiroaki Tatsumi [b], Atsushi M Ito [c,d], Arimichi Takayama [c,d], Takeshi Wada [e], Hidemi Kato [e], Hiroshi Nisikawa [b,**]

[a] Graduate School of Engineering, The University of Osaka, 2-1 Yamadaoka, Suita, Osaka 565-0871, Japan
[b] Joining and Welding Research Institute, The University of Osaka, 11-1 Mihogaoka, Ibaraki, Osaka 567-0047, Japan
[c] National Institute for Fusion Science, Natural Institutes of Natural Sciences, 332-6 Oroshityo, Toki, Gifu 509-5202, Japan
[d] Graduate Institute for Advanced Studies, SOKENDAI, 332-6 Oroshityo, Toki, Gifu 509-5202, Japan
[e] Institute for Materials Research, Tohoku University, 2-1-1 Katahira, Sendai, Miyagi 980-8577 Japan

ARTICLE INFO

Keywords:
Surface modification
Sn–In composite alloys
Mechanical Properties
Adsorption energy
Density functional theory

ABSTRACT

We focus on the role of surface modification of nanoparticles employed as reinforcements in Sn–52mass %In composite alloys (the alloys), and how these surface differences affect the microstructure and mechanical properties of the alloys. Microscopic observation revealed that the addition of surface–modified ZrO_2 nanoparticles (ZrO_2 NPs) by NiO (NiO/ZrO_2 NPs) led to a finer γ-phase spacing compared to alloys containing unmodified ZrO_2 NPs. This is attributed to enhanced heterogeneous nucleation promoted by the surface modification. Nanoindentation tests showed that the microhardness of the alloys was increased by 5.7 MPa upon NP surface modification, suggesting microstructural refinement caused by surface modification and subsequent changes in the free energy of heterogeneous nucleation. Density functional theory calculations demonstrated that NiO/ZrO_2 surfaces exhibit lower ensemble average of adsorption energies for the alloys adatoms than that exhibited by ZrO_2 surfaces, with energy minima aligning with the lattice periodicity of the β–phase or γ–phase. These findings suggest that the surface modification induces a crystallization preference during solidification, thereby improving the alloy properties. This work highlights the impact of NP surface modification-induced changes in nucleation energetics on the solidification behavior and mechanical properties of the alloys, providing insights for electronic packaging material design.

1. Introduction

The development of advanced technologies such as artificial intelligence has increased data processing volumes, while the semiconductor devices that support data processing continue to miniaturize year after year making further miniaturization challenging [1]. Three-dimensional packaging is therefore attracting attention as a new electronic packaging technology [1–3]. Three-dimensional packaging requires soldering with varying melting temperatures, such as low-temperature solder for stacking. Specifically, the melting temperature of the solder at the first level is the highest, which ensures that the first-level solder joints do not melt while the second-level joints are being processed [4,5]. The demand for low-temperature solder is increasing to minimize thermal effects on the joint [6,7]. Moreover, flexible electronic devices can easily fit into complex shapes [8,9], comprising flexible substrates composed of thin heat-sensitive resin films [10]. Although such flexible substrates show good versatility for a wide variety of flexible devices, their temperature tolerance remains a major issue, especially against high-temperature exposure during the soldering process. According to Zardetto et al. [11], the electrical resistance of a flexible substrate increase markedly when the temperature exceeds 180°C. Sn–Ag–Cu solder (SAC) is widely used as Pb-free solder, and the peak temperature during soldering typically reaches approximately 250°C [12,13]. Among various low-temperature solder alloys, Sn–58Bi eutectic solder is widely used due to its relatively low melting point of 138 °C, good mechanical properties, and cost-effectiveness. However, its melting point is still

* Corresponding author at: Graduate School of Engineering, Osaka University, 2-1 Yamadaoka, Suita, Osaka 565-0871, Japan.
** Corresponding author at: Joining and Welding Research Institute, Osaka University, 11-1 Mihogaoka, Ibaraki, Osaka 567-0047, Japan.
E-mail addresses: nitta.shunya.gvc@ecs.osaka-u.ac.jp (S. Nitta), tatsumi.jwri@osaka-u.ac.jp (H. Tatsumi), ito.atsushi@nifs.ac.jp (A.M. Ito), takayama.arimichi@nifs.ac.jp (A. Takayama), takeshi.wada.d7@tohoku.ac.jp (T. Wada), hikato@imr.tohoku.ac.jp (H. Kato), nisikawa.jwri@osaka-u.ac.jp (H. Nisikawa).

https://doi.org/10.1016/j.surfin.2026.108793
Received 16 October 2025; Received in revised form 1 February 2026; Accepted 13 February 2026
Available online 14 February 2026

close to the thermal deformation threshold of polymer-based substrates such as PET and PI, which are commonly used in flexible electronics. Zardetto et al. [11] reported that PET substrates begin to exhibit dimensional instability above 130–150 °C, and Wu et al. [14] suggested that Sn–58Bi solder may be insufficient for polymer-based substrates. Therefore, alternative solder alloys with lower melting points are needed for applications involving temperature-sensitive components.

Sn–52mass %In alloy (Sn–In alloy) is a promising low melting temperature solder. The eutectic Sn–In alloy shows a significantly low melting temperature of 119°C [15]. However, the low tensile strength of Sn–In alloys is a critical issue. Han et al. [16] reported that the ultimate tensile strength of the eutectic Sn–In alloy was approximately 11.0 MPa, which is lower than that of Sn–3.0mass %Ag–0.5mass %Cu alloy (41.6 MPa) [17], which necessitates improving the ultimate tensile strength of the alloy.

The addition of nanoparticles (NPs) to solder alloys has been actively investigated as a promising approach for improving their strength [18–20]. Recent studies have highlighted the role of ZrO_2 nanoparticles in enhancing the performance of Sn–Ag–Cu solder alloys. Skwarek et al. [3] demonstrated that the incorporation of ZrO_2 nanoparticles leads to microstructural refinement and improved mechanical properties, supported by both experimental and theoretical analyses. Similarly, Rajendran et al. [4] reported that ZrO_2 reinforcement in SAC305 solder joints significantly increases shear strength and influences aging behavior, underscoring the importance of nanoparticle size in determining joint reliability.

However, the high surface energy of nanoparticles often leads to their aggregation within the alloy matrix. To overcome this, surface modification of nanoparticles has been proposed as an effective strategy. Huo et al. [21] reported that ZrO_2 nanoparticles coated with a NiO layer (NiO/ZrO_2 NPs) exhibited a uniform dispersion within a Sn–1.0Ag–0.5Cu solder matrix. In our previous study [22], the addition of NiO/ZrO_2 NPs increased the tensile strength of Sn–In composite alloys by approximately 37 %. However, the mechanism for the enhanced dispersibility through surface modification remains unclear.

This study aims to elucidate the effects of surface-modified nanoparticle on the refinement of microstructure and strengthening in composite solder alloys. We prepared composite alloys with ZrO_2 NPs or NiO/ZrO_2 NPs and conducted microstructural observations and microhardness tests. We discussed the interaction between the NPs surfaces, which are considered as heterogeneous nuclei, and the solder alloy during the solidification process. First-principles calculations using density functional theory (DFT) were also performed.

2. Methods

2.1. Experiments

2.1.1. Fabrication of Sn–In alloy composite alloys

Sn–In composite alloys with ZrO_2 and NiO/ZrO_2 NPs were fabricated. The NiO/ZrO_2 NPs were prepared by ball-milling pyrolysis using ZrO_2 NPs (HW Nanomaterials, China) and $Ni(CH_3COO)_2{\cdot}4H_2O$ (Wako Pure Chemicals Corporation, USA) as raw materials. The ZrO_2 NPs (99.9 % purity) had a particle size distribution of 60–120 nm. NiO NPs (99.9 % purity), approximately 8.8 nm in size, were uniformly and densely attached to the surface of the ZrO_2 NPs. The detailed procedure of the ball-milling pyrolysis was described in our previous report [23]. The prepared nanoparticles were characterized using the Brunauer–Emmett–Teller (BET) method to evaluate their specific surface area and BET equivalent diameter. The BET results showed that ZrO_2 nanoparticles exhibited a specific surface area of 1.4 m^2/g and a calculated equivalent diameter of 750 nm, whereas NiO/ZrO_2 nanoparticles exhibited 3.2 m^2/g and 320 nm, respectively.

A schematic of the fabrication process for the composite alloy is presented in Fig. 1. Approximately 30 *g*of the commercial Sn–In alloy (Senju Metal Industry Corporation, Japan) (99.9 % purity) was heated to 250°C in a furnace in air, as shown in Fig. 1(a). After melting, ZrO_2 or NiO/ZrO_2 NPs were introduced at mass fractions of 0 or 0.4 mass %, as shown in Fig. 1(b). An ultrasonic homogenizer THU–80 (Taiyo Corporation, Japan) with an output power of 80 W, a frequency of 20 kHz, and a tip diameter of 1/8 inch was then applied to the mixture consisting of the molten alloy and each nanoparticle for 240 s, as shown in Fig. 1(c). After removing the oxide film from the molten alloy surface, the molten alloy was cast into an iron mold (50 mm × 10 mm × 5 mm) that had been sufficiently cooled prior to casting to ensure rapid and consistent solidification across all samples.

2.1.2. Microstructural observation

The microstructures of the cross-sectioned Sn–In composite alloys were observed by scanning electron microscopy (SEM, JSM-IT200, JEOL, Japan). Prior to observation, the samples were ground sequentially with SiC papers in the order of #800, #1200, and #2000 and polished with 1.0 and 0.3 μm alumina suspensions. The Sn–In alloy is known to consist of two phases, γ and β [22]. Previous studies have reported that the γ phase exhibits a higher hardness than the β phase, and that the spacing between hard phases strongly influences the local microhardness of the alloy [24]. Based on these findings, the present study evaluates the correlation distance of the γ phase. For the purpose, a test line was drawn on each microstructural image, and the number of intersections between the γ-phase and the line was counted to quantify the phase spacing using the ImageJ image-analysis software [25]. For each condition, two microstructural images were analyzed, and a total of 20 test lines (10 lines per image) were drawn to determine the phase spacing.

2.1.3. Nanoindentation test

Nanoindentation tests were performed to evaluate the microhardness of the Sn–In composite alloys with ZrO_2 and NiO/ZrO_2 NPs. The tests were carried out at 30°C on polished Sn–In composite alloys using a nanoindentation tester (ENT-5/ELIONIX-5, ELIONIX Inc.) with a Berkovich indenter tip. The maximum indentation load was 20 mN and the holding time at maximum load was 30 s to minimize the effect of initial

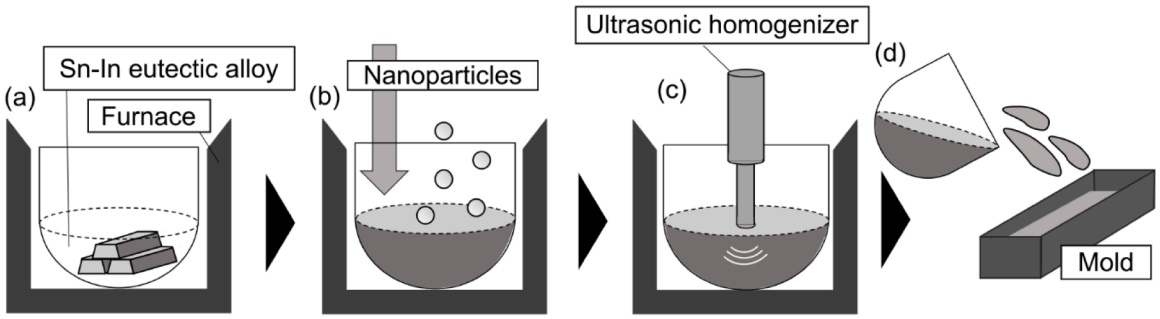

Fig. 1. Schematic of the (a) melting, (b) nanoparticle addition, (c) agitation, and (d) casting process.

creep.

During each indentation experiment, load versus indentation displacement response of the solder material in the direction normal to the cross-sectional surface was measured. For each Sn–In composite alloy, 10 nanoindentation tests were performed and the mean values and standard deviations were calculated.

2.2. DFT simulations

2.2.1. Computational framework

In order to evaluate the adsorption energy of solder alloy atoms on target nanoparticles, the DFT simulation was carried out. The wave function for the electrons bound by atomic nuclei is numerically solved on the Kohn-Sham equation [26,27] by using the OpenMX (Open source package for Material eXplorer) [28] code. In the code, only valence electrons were explicitly simulated under frozen core approximation and norm-conserving pseudo-potentials. Here, the pseudo-potentials model is Morrison-Bylander-Kleinman type model [29]. The generalized gradient approximation (GGA) with a Perdew-Burke-Ernzerhof (PBE) functional [30] was employed as an exchange-correlation potential. Valence electron orbitals are represented as a linear combination of atomic orbitals (LCAO). In OpenMX, these atomic orbitals are pseudo-atomic orbitals (PAOs), which is numerically generated from spherically symmetric DFT calculation and are consistent with the corresponding pseudo-potentials [31,32]. OpenMX employs norm-conserving MBK-type pseudopotentials together with the corresponding pseudo-atomic orbitals (PAOs). These pseudopotentials, whose formulation is comparable to optimized norm-conserving Vanderbilt (ONCV) types [33], accurately describe valence and near-valence electronic states. The PAO–pseudopotential combinations in the standard OpenMX library have been benchmarked against all-electron methods such as Wien2k, demonstrating plane-wave-level accuracy and satisfactory delta-gauge performance [34,35] when an energy-cutoff-equivalent real-space grid is used. Therefore, the selected s-, p-, d-, and f-type PAOs for Sn, In, Ni, O, and Zr appropriately represent the electronic states relevant to bonding and charge-transfer processes at the nanoparticle surface. We employed: the 2 s-states, 2 p-states, 3 d-states, and 1 f-state of radial orbital functions with a cut-off radius of 7.0 a.u. for Sn, the 2 s-states, 2 p-states, 2 d-states, and 1 f-state of radial orbital functions with a cut-off radius of 7.0 a.u. for In; the 3 s-states, 3 p-states and 2 d-states radial orbital functions with a cut-off radius of 6.0 a.u. for Ni; the 2 s-states, 2 p-states and 1 d-state radial functions with a cut-off radius of 7.0 a.u. for O; and the 3 s-states, 3 p-states, 3 d-states, and 1 f-state of radial orbital functions with a cut-off radius of 7.0 a.u. for Zr. The cutoff energy was set to 250 Ry and k-point grids were set to $4 \times 4 \times 1$ sampling in the Brillouin zone. The OpenMX calculations were efficiently performed by using improvement for the vector architecture processor super computer [36].

2.2.2. Calculation model

Figs. 2 and 3 show the prepared surface slab models. The lattice parameter of ZrO_2 are $a = b = 0.52$ and $c = 0.53$ nm and the space group is P21/C [37]. The surface orientation was chosen to be (1 -1 1), the closest–packed plane, with the expectation of minimum surface energy. Meanwhile, the lattice parameter of NiO are $a = b = c = 0.42$ nm and the space group is Fm-3 m [38]. The interfacial orientation was chosen to be (0 0 1), the closest–packed plane, with the expectation of minimum surface energy. A $2 \times 2 \times 2$ supercell was selected for both crystal structures. Moreover, 1.5 nm thick vacuum layers were inserted into these surface slab models to ensure no significant interaction between the slab models in the c-axis direction. Fig. 4 shows the adsorption model for calculating the adsorption energy between the surface slab model of nanoparticles and the Sn or In adatom. The Sn or In adatom was placed on top of the surface slab model of the NP.

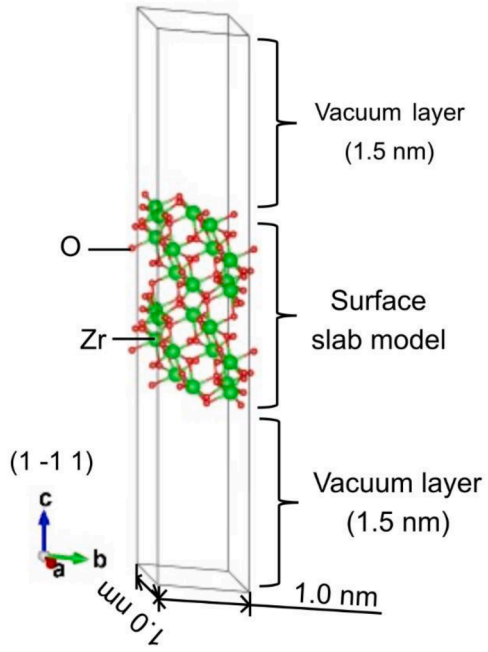

Fig. 2. ZrO_2 surface slab model used in this study.

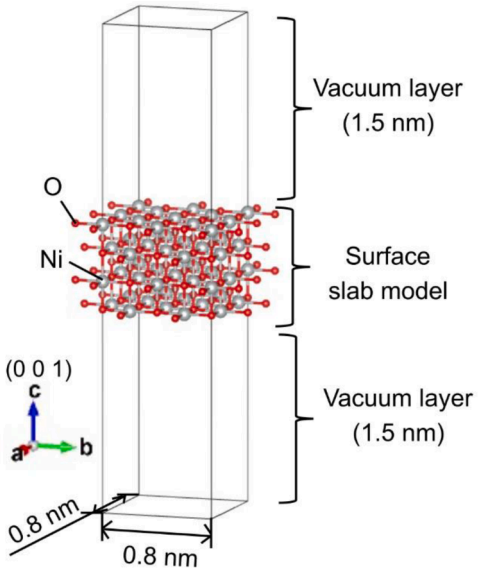

Fig. 3. NiO surface slab model used in this study.

2.2.3. Adsorption energy calculation

The adsorption energies for solder alloy atoms on target nanoparticles E_{ab} were calculated using the following equations [39]:

$$E_{ad} = E_{all} - (E_a + E_b) \tag{7}$$

where E_{all} is the total energy of the adsorption state, E_a is the total energy of the independent atomic state of a solder alloy atom Sn or In, and E_b is the total energy of the surface slab state of ZrO_2 or NiO. To ensure the reliability of the adsorption energy evaluations, structural relaxation of the surface slab models was carried out prior to the calculations. In the adsorption state, the z-coordinate of the adatom Sn or In was relaxed and but x- and y-coordinates were fixed in the calculation. The calculations were performed with 81 points from equally spaced 9×9 grids. The adsorption energies obtained were mapped by trigonometric interpolation. Furthermore, the adsorption probability of the Sn or In

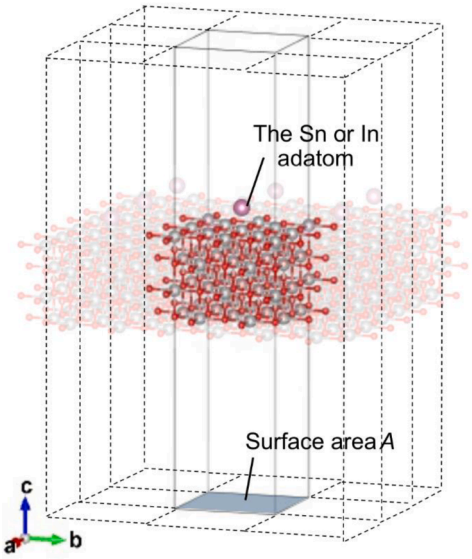

Fig. 4. Adsorption model with surface slab model of the Sn or In adatom on NiO.

adatom is not expected to be uniform across the nanoparticle surface based on the potential energy surface. In the canonical ensemble at a temperature T, the probability distribution function for x- and y-coordinates of an adatom, $P(x,y)$, of the potential energy E is given by [40, 41]

$$P(x,y) = \frac{\exp(-E(x,y)/k_BT)}{\sum_{\substack{i=0\\j=0}} \exp(-E_{i,j}/k_BT)} \tag{8}$$

where P_n is the probability of existence of the adatoms at each coordinate, $E(x,y)$ is the adsorption energy at each coordinate, k_B is Boltzmann's constant and T is absolute temperature. From this distribution function, the ensemble mean, which is the expected value of the adsorption energy, is obtained from the following equation [40].

$$\langle \alpha \rangle = \frac{\iint E(x,y)\exp\left(-\frac{E(x,y)}{k_BT}\right)dxdy}{\iint \exp\left(-\frac{E(x,y)}{k_BT}\right)dxdy} = \frac{\sum_{\substack{i=0\\j=0}} E_{i,j}\exp\left(-\frac{E_{i,j}}{k_BT}\right)}{\sum_{\substack{i=0\\j=0}} \exp\left(-\frac{E_{i,j}}{k_BT}\right)} \tag{9}$$

3. Results and discussion

3.1. Microhardness

To interpret the nanoindentation results, the microstructure of the Sn–In composite alloy was examined by SEM (high magnification) and OM (low magnification), as shown in Figs. 5 and 6. Two phases with convex and covering morphologies were observed in the Sn–In composite alloy regardless of the observation methods. To compare the effect of nanoparticle addition on microstructure refinement, the phase spacing of the γ phase in the SEM images was measured. The average phase spacing of the γ phase of the Sn–In composite alloy without NPs was 15.2 μm. Meanwhile, the average phase spacing of that with ZrO_2 NPs and NiO/ZrO_2 NPs were measured as 8.55 μm and 5.46 μm. SEM images show that the phase spacing of the Sn–In composite alloy with NiO/ZrO_2 NPs is smaller than that of the Sn–In composite alloy with ZrO_2 NPs. Furthermore, OM images of the Sn–In composite alloy were shown in Fig. 6. The image of the Sn–In composite alloys with ZrO_2 in Fig. 6 (a) shows some areas of coarse γ phase as indicated by dotted circles. Meanwhile, that of the Sn–In composite alloys with NiO/ZrO_2 NPs was relatively homogeneous. Therefore, surface modification of nanoparticles homogenizes the microstructure.

Fig. 7 shows an OM image of an indentation in the microstructure of Sn–In alloys. A maximum load of 20 mN was selected for the tests so that the indentation marks were large enough to cover both phases of the Sn–In alloys. Thus, the nanoindentation tests characterized the macroscopic mechanical properties of the Sn–In alloys, rather than the localized properties in the γ (Sn_4In) or β phase ($SnIn_3$) in the eutectic phases. Fig. 8 shows a typical measured load–depth curve of the Sn–In alloy, Sn–In composite alloy with ZrO_2 NPs and Sn–In composite alloy with NiO/ZrO_2 NPs. The indentation depth of the Sn–In alloy was the largest, followed by that of the Sn–In composite alloy with ZrO_2 NPs. Finally, the indentation depth of the Sn–In composite alloy with NiO/ZrO_2 NPs was the smallest. The microhardness of the Sn–In composite alloy with NiO/ZrO_2 NPs was the highest. Fig. 9 show the average microhardness and standard deviation of the Sn–In alloy, Sn–In composite alloy with ZrO_2 NPs, and Sn–In composite alloy with NiO/ZrO_2 NPs. The average microhardness of the Sn–In alloy was 40.5 MPa with a standard deviation of 3.6 MPa. The microhardness of the Sn–In composite alloys increased by 7.6 % with the addition of ZrO_2 NPs and 21.7 % with the addition of NiO/ZrO_2 NPs. Therefore, the addition of NPs to the Sn–In alloy increased the microhardness.

There are two possible reasons for the increase in microhardness of Sn–In alloys by NP addition. The increased microhardness can be attributed to the pinning effect of the nanoparticles and refinement of the hard phase (γ–Sn_4In). Amares et al. [42] showed that the strength of a Sn–Bi eutectic solder increased with the addition of ZrO_2 nanoparticles due to alloy matrix refinement and strengthened ZrO_2–nanoparticle dispersion. Xing et al. [43] also reported that an increase in the pinning effect and dislocation density because of the addition of nanoparticles and the linear motion of dislocations. Moreover, Hong et al. found that the addition of 0.5 mass % nanoparticles of which 75 % AlN and 25 % Al to Mg-based alloys resulted in the refinement of the eutectic phase and improved shear strength [44]. Furthermore, the microhardness of Sn–In composite alloys with NiO/ZrO_2 NPs was harder than that of Sn–In composite alloys with ZrO_2. Thus, surface modification of NPs may play an important role in increasing microhardness.

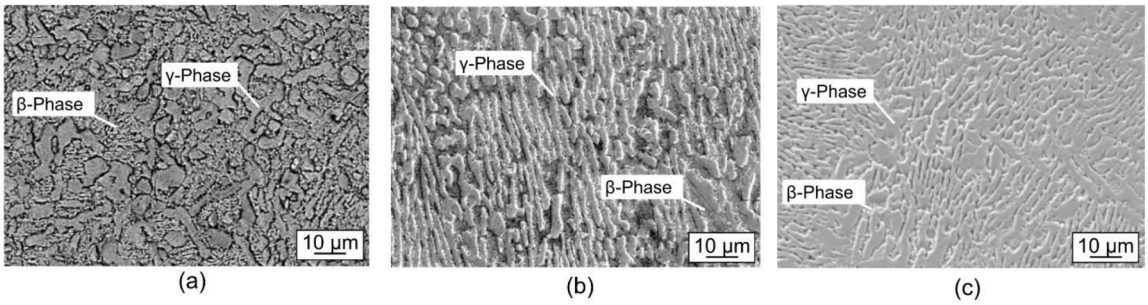

Fig. 5. SEM microstructure images of the Sn–In composite alloys with (a) without NPs (b) with ZrO_2 NPs and (c) NiO/ZrO_2 NPs.

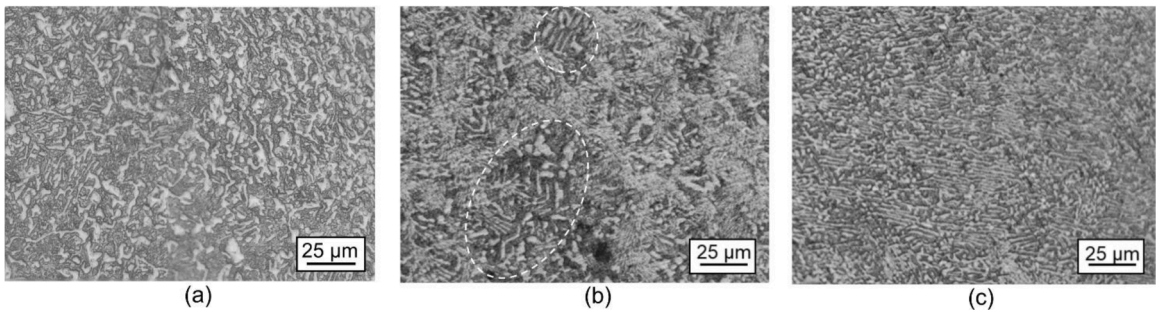

Fig. 6. OM microstructure images of the Sn–In composite alloys (a) without NPs (b) with ZrO_2 NPs and (c) NiO/ZrO_2 NPs.

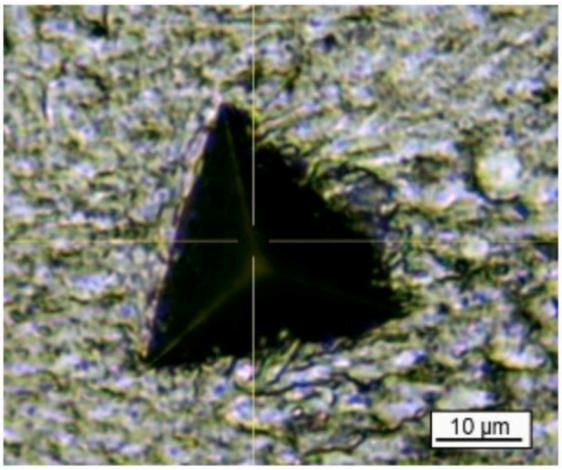

Fig. 7. Representative indentation of the Sn–In alloy by nanoindentation.

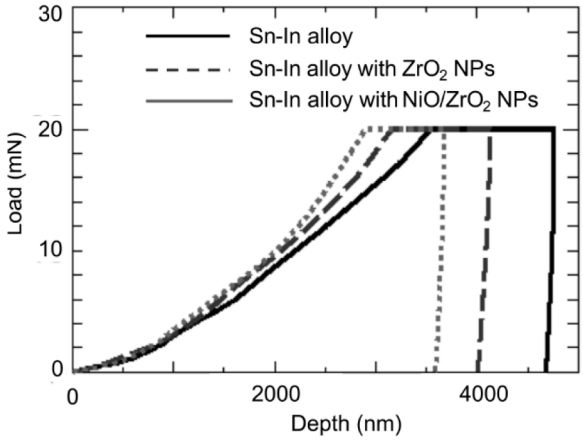

Fig. 8. Representative Load–Depth diagram of the Sn–In alloy, the Sn–In composite alloy with ZrO_2 NPs, and the Sn–In composite alloy with NiO/ZrO_2 NPs by nanoindentation.

3.2. Effect of surface modification on microstructure of alloys

SEM and OM observations show that the addition of surface-modified nanoparticles results in a more homogeneous and finer Sn–In alloy microstructure compared to the use of non-surface-modified nanoparticles. Previous studies have shown that nanoparticle addition to solder alloys leads to a fine microstructure. However, the effect of surface modification of the nanoparticles has not been clarified. In this section, the effects of surface modification are discussed from two perspectives: (i) improved particle dispersion due to enhanced wettability and (ii) promotion of heterogeneous nucleation.

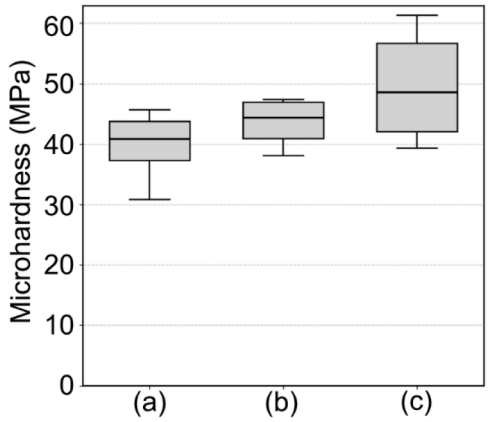

Fig. 9. Box–and–whisker plot of the microhardness for the (a) Sn–In alloy, (b) Sn–In composite alloy with ZrO_2 NPs, and (c) Sn–In composite alloy with NiO/ZrO_2 NPs by nanoindentation.

The dispersibility of nanoparticles in molten alloys has already been discussed by Chen et al. [45]. They reported that three energies are important for nanoparticles to become homogeneously dispersed and self-stabilizing in molten metal: minimum van der Waals potential for maximum attraction; the energy barrier due to the interfacial energy; and the thermal energy [45]. Among them, energy barriers that depend on interfacial energy are reported to be at least 2000 times more effective than thermal energy. Considering that the van der Waals potential is highly dependent on the interparticle distance, the energy barrier due to the interfacial energy is critically important for achieving homogeneous nanoparticle dispersion in molten alloys. This interfacial energy between the NPs and molten solder in this study is given as follows [45]:

$$W_{\text{barrier}} = S(\sigma_{\text{NP}} - \sigma_{\text{NP-Solder}}) = S\sigma_{\text{solder}}\cos\theta \quad (1)$$

where S is the effective area, σ_{NP} is the surface energy of nanoparticles, $\sigma_{\text{NP-Solder}}$ is the interfacial energy between nanoparticles and molten solder, σ_{solder} is the surface tension of molten solder, and θ is the contact angle of molten solder on the nanoparticle surface. The wettability between ZrO_2 and Sn–based alloys is known to be unfavorable, and physical vapor deposition or ultrasonic irradiation is required to improve wettability [46–48]. Meanwhile, Eustathopoulos et al showed that the wetting angle at the NiO/Sn interface is about 30°, indicating that Sn and NiO are reactive [49]. Lin et al. also explained that NiO is reduced based on the following reaction equation because the Gibbs free energy of reaction is negative [50].

$$\text{Sn} + 2\text{NiO} \rightarrow \text{SnO}_2 + \text{Ni} \quad (2)$$

Therefore, NiO has a smaller contact angle with the solder alloy than ZrO_2. The difference in wetting angles between the nanoparticle surfaces

and molten solder alloy may have resulted in the homogeneous dispersion of the nanoparticles and homogeneous microstructure of the Sn–In composite alloys. This interfacial reaction occurs during melting and solidification processes, and the NiO layer used for surface modification is extremely thin; therefore, the amount of SnO_2 formed is expected to be minimal and would not affect the properties of the solder alloy.

The enhancement of the refinement effect by surface modification of nanoparticles can be considered from the perspective of promotion of heterogeneous nucleation. Heterogeneous nucleation on the substrate has conventionally been considered in the classical model where the crystal nucleus in the form of a spherical cap, shown in Fig. 10, formed a contact angle θ with the substrate. In Fig. 10, γ_{LS} is defined as the free energy at the liquid/solid interface, γ_{SN} as the free energy at the solid/nucleus interface and γ_{LN} as the free energy at the liquid/nucleus interface. The relationship of these energies with the contact angle θ is given below [45,51].

$$\gamma_{LS} = \gamma_{SN} + \gamma_{LN}\cos\theta \tag{3}$$

The free energy of heterogeneous nucleation ΔG_{hetero} can be expressed using the free energy of homogeneous nucleation ΔG and contact angle θ as follows [52,53]

$$\Delta G_{hetero} = \Delta G \cdot f(\theta) \tag{4}$$

$$\Delta G = 4\pi r^2 \gamma_{LN} - \frac{4}{3}\pi r^3 \Delta\mu_V \tag{5}$$

$$f(\theta) = \frac{1}{4}\left(2 - 3\cos\theta + \cos^3\theta\right) \tag{6}$$

where r is the radius of the nucleation site and $\Delta\mu_V$ is the change in free energy with solidification of the alloys. This equation indicates that understanding θ and γ_{LN} is important for the free energy of heterogeneous nucleation, considering that $\Delta\mu_V$ depends on the composition of the alloys. For this study, the contact angle in the system is expected to be smaller at the NiO/Sn interface, as indicated in the previous paragraph. However, the interfacial energies of NiO and ZrO_2 for Sn–In alloys are not known.

To accurately consider the grain refinement effect, the interfacial energy between the nanoparticle surface and alloy must be understood. However, existing experimental methods to obtain interfacial energies directly are unreliable [54]. Recently, first-principles calculations based on DFT have been used to calculate interfacial energies. In a previous work, the interfacial energy and adhesion work of liquid Ag on yttria stabilized zirconia (YSZ) are calculated using DFT with a model of Ag atoms clustered on the crystal structure of YSZ [55]. As a result, the interfacial products in brazing are clarified. Even more surprising is the fact that the superiority of the interfacial energy does not change whether the liquid phase is a cluster or a single atom, according to the calculations of Gangotri et al. [56]. This suggests that a single atom is sufficient for the liquid phase when comparing the interfacial energies of the solder alloys to the NiO and ZrO_2 nanoparticle surfaces. In the next section, the method for calculating the adsorption energy between the nanoparticle surface and the Sn–In alloy is presented. The adsorption energy using DFT is a reliable indicator of the interfacial energy

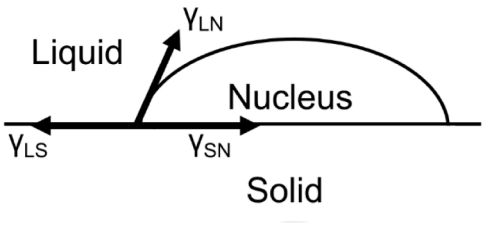

Fig. 10. Diagram of heterogeneous nucleation and the role of each energy.

[44–46].

3.3. Calculation of adsorption energy

Adsorption energy maps of the Sn and In adatom were calculated for both NiO and ZrO_2 surface models, as shown in Fig. 11. These maps visualize the variation in adsorption energy across the x–y plane of the surface slabs. Fig. 11(a) and 11(b) show the adsorption energy distributions for Sn/NiO and In/NiO, respectively, while Fig. 11(c) and 11(d) correspond to that of Sn/ZrO_2 and In/ZrO_2. In these maps, the blue regions indicate low adsorption energy (i.e., thermodynamically favorable sites for adsorption), and yellow regions represent high energy regions (unfavorable sites for adsorption). In the NiO models (Fig. 11(a) and (b)), the adsorption energy is negative across all regions, indicating spontaneous adsorption of the Sn or In adatom. Several energy minima are periodically distributed across the surface, located near the centers of squares formed by four adjacent atoms. The distance between the periodically arranged minima is approximately 0.3 nm, which may play an important role in the structure formation following atomic adsorption. In contrast, in the ZrO_2 models (Fig. 11(c) and (d)), the adsorption energy is positive in some regions, suggesting that the Sn or In adatom is unlikely to adsorb spontaneously. Additionally, the local minima are irregularly distributed with no apparent periodicity.

Fig. 12(a) presents the crystal structure of the γ–phase of the Sn–In alloy along with its interatomic distances. The measured distances are 0.44 nm along the [001] direction, 0.35 nm along [100], and 0.33 nm along [111]. Compared with the distance of minima calculated on the adsorption model with NiO (~0.3 nm) shown in Fig. 11(a) and (b), these values correspond to relative differences of +46 %, +16 %, and +10 %, respectively. Among these, the [111] direction shows the smallest deviation, suggesting a partial geometric compatibility between the γ–phase and the periodic minima on the NiO surface. Fig. 12(b) shows the crystal structure of the β–phase. The interatomic distances are 0.30 nm along [001] and 0.32 nm along [100], corresponding to deviations of 0 % and +7 % from the distance of minima calculated on the adsorption model with NiO. This close match indicates a high degree of structural compatibility between the β–phase and the NiO surface adsorption sites. Such geometric compatibility can lower the energy barrier for epitaxial growth and promote heterogeneous nucleation during solidification.

Table 1 summarizes the average adsorption energies and the ensemble averages of the Sn and In adatom on NiO and ZrO_2 surfaces, as obtained from the adsorption energy maps shown in Fig. 11. These values quantitatively compare the thermodynamic stability of adatom adsorption on different nanoparticle surfaces. As shown in Table 1, in terms of both average adsorption energy and ensemble average, the adsorption energies of the Sn or In adatom are lower on the NiO surface than on ZrO_2. The ensemble averages indicate that NiO–modified surfaces provide energetically more favorable environments for adatom adsorption, thereby favoring nucleation compared to ZrO_2 surfaces. Additionally, Eustathopoulos explained that NiO exhibits a smaller wetting angle with Sn compared to ZrO_2, suggesting better wettability and lower interfacial energy [57]. By substituting these values into Eq. (5) implies that the presence of NiO/ZrO_2 nanoparticles significantly reduces the free energy barrier (ΔG) for heterogeneous nucleation, which may enhance nucleation rates and lead to microstructural refinement. According to classical nucleation theory and the work of Sosso et al. [58], the nucleation rate J is expressed as:

$$J = J_0 \exp\left(-\frac{\Delta G}{k_B T}\right) \tag{6a}$$

where k_B is Boltzmann constant and J_0 is the prefactor. Surface modification of the nanoparticles is expected to lower the nucleation energy barrier ΔG, which, as shown in Eq. (6), increases the nucleation rate J. A higher nucleation rate can promote more frequent phase transformations during solidification, contributing to a finer microstructure.

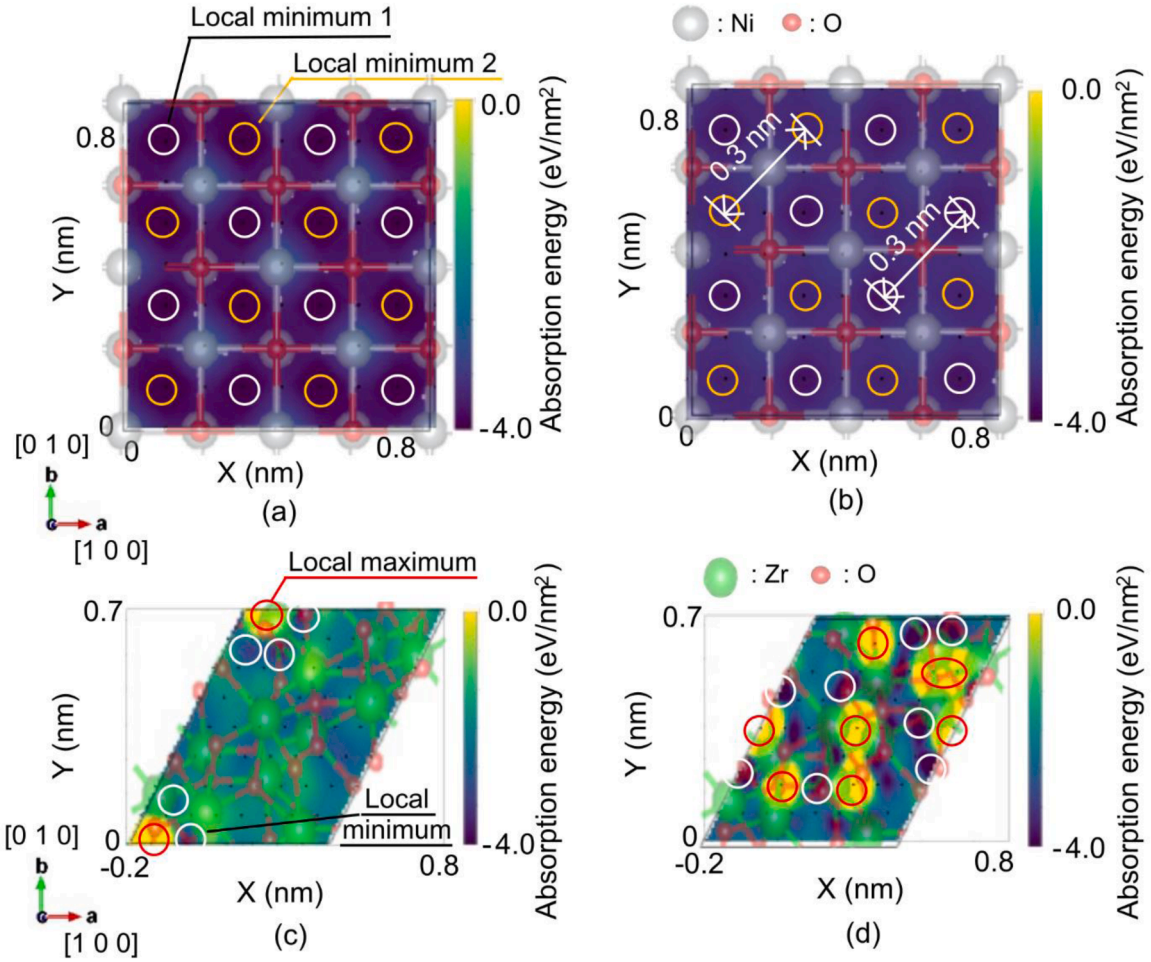

Fig. 11. Energy maps of the adsorption energy of the single adatom constituting Sn–In alloys on the crystal structure of nanoparticles: (a) Sn/NiO (b) In/NiO (c) Sn/ZrO_2 (d) In/ZrO_2.

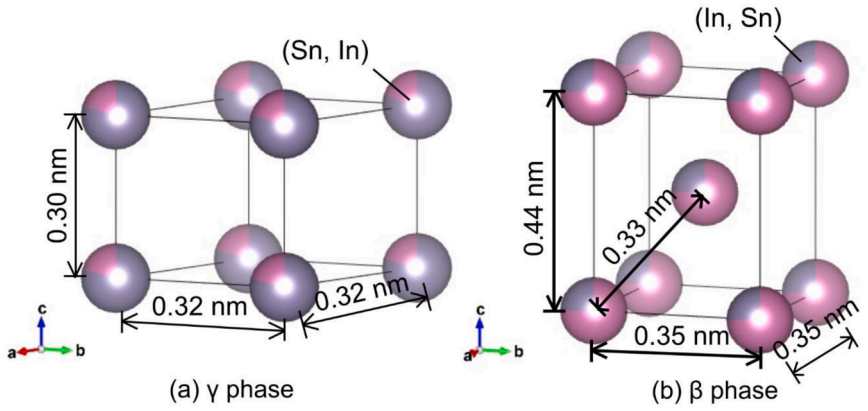

Fig. 12. Crystal structure of the (a) γ and (b) β phase in the Sn–In alloys with their interatomic distances.

Furthermore, enhanced nucleation kinetics may activate more nanoparticles as effective nucleation sites, further amplifying microstructural refinement. It should be noted that, although heterogeneous nucleation promoted by surface-modified nanoparticles appears to be the dominant mechanism in the present system, the possible contribution of other solidification mechanisms—such as the inhibiting the migration of grain boundaries and local solute redistribution caused by the adsorption of molten atoms onto their surfaces—cannot be completely excluded.

4. Conclusion

We clarified the effects of surface modification of nanoparticles on the microstructure and microhardness of Sn–In composite alloys through experiments and simulations. The microhardness of the composite alloy increased upon NP surface modification owing to the refinement of the hard phase with the decrease in the phase spacing of γ phase. The thermodynamic origin of heterogeneous nucleation was further explored using DFT. The ensemble average of adsorption energy

Table 1
Average interface energies and ensemble average of adsorption energies obtain from Fig. 11.

Calculation model	Average adsorption energy [eV]	Ensemble average of adsorption energy [eV]
Sn/NiO	–2.56	–2.92
In/NiO	–2.42	–2.60
Sn/ZrO_2	–0.75	–1.44
In/ZrO_2	–0.10	–1.51

was consistently lower on NiO surfaces, indicating a thermodynamically more favorable environment for nucleation. Moreover, the NiO surfaces exhibited periodic adsorption energy minima, with inter-minimum distances closely matching the interatomic spacings of the γ (Sn_4In) and β phases ($SnIn_3$) of the Sn–In alloy. This structural correspondence implies a crystallographic preference for nucleation on NiO, which may contribute to a reduction in the free energy barrier for heterogeneous nucleation. In addition, the reduction in interfacial energy enhanced the wettability of the nanoparticles, promoting a more homogeneous dispersion of NiO/ZrO_2 nanoparticles within the molten alloy. These findings demonstrate that nanoparticle surface modification significantly impacts the solidification behavior of Sn–In alloys. The enhanced nucleation kinetics and resultant microstructure refinement contribute to improved mechanical properties, offering valuable insights into the design of high-performance alloy materials. This work underscores the potential of surface-engineered nanoparticles in tailoring the properties of composite alloys for advanced electronic packaging applications. However, the scope of this study is limited to NiO/ZrO_2 nanoparticles and a specific Sn–In alloy system. The influence of other nanoparticle chemistries and surface modification remains to be explored. Future research should aim to expand the range of nanoparticle types to further elucidate the mechanisms governing heterogeneous nucleation and microstructural evolution. These efforts will be essential for advancing composite alloy design in electronic packaging applications under increasingly demanding service conditions.

Declaration of generative AI and AI-assisted technologies in the manuscript preparation process

During the preparation of this work, the authors used Microsoft Copilot in order to assist with language refinement. After using this tool, the authors reviewed and edited the content as needed and take full responsibility for the content of the published article.

Data statement

The data that support the findings of this study are available from the corresponding author upon reasonable request.

CRediT authorship contribution statement

Shunya Nitta: Writing – original draft, Visualization, Methodology, Investigation, Conceptualization. **Hiroaki Tatsumi:** Writing – review & editing, Supervision. **Atsushi M Ito:** Software, Methodology. **Arimichi Takayama:** Software, Methodology. **Takeshi Wada:** Writing – review & editing. **Hidemi Kato:** Writing – review & editing. **Hiroshi Nisikawa:** Writing – review & editing, Supervision.

Declaration of competing interest

The authors declare that they have no known competing financial interests or personal relationships that could have appeared to influence the work reported in this paper.

Acknowledgements

This work was partly supported by the Project on Design & Engineering by Joint Inverse Innovation for Materials Architecture (DEJI2MA) from the Ministry of Education, Culture, Sports, Science and Technology (MEXT). DFT is performed on "Plasma Simulator" (NEC SX-Aurora TSUBASA) of NIFS with the support and under the auspices of the NIFS Collaboration Research program (NIFS23KISS034).

References

[1] S.Q. Gu, Material innovation opportunities for 3D integrated circuits from a wireless application point of view, MRS Bull. 40 (2015) 233–241, https://doi.org/10.1557/mrs.2015.9.
[2] A.W. Topol, D.C.L. Tulipe, L. Shi, D.J. Frank, K. Bernstein, S.E. Steen, A. Kumar, G. U. Singco, A.M. Young, K.W. Guarini, M. Ieong, Three-dimensional integrated circuits, IBM J. Res. Dev. 50 (2006) 491–506, https://doi.org/10.1147/rd.504.0491.
[3] J.U. Knickerbocker, P.S. Andry, B. Dang, R.R. Horton, C.S. Patel, R.J. Polastre, K. Sakuma, E.S. Sprogis, C.K. Tsang, B.C. Webb, S.L. Wright, 3D silicon integration, in: 2008 58th Electronic Components and Technology Conference, 2008, pp. 538–543, https://doi.org/10.1109/ECTC.2008.4550025.
[4] Y. Liu, K.N. Tu, Low melting point solders based on Sn, Bi, and In elements, Mater. Today Adv. 8 (2020) 100115, https://doi.org/10.1016/j.mtadv.2020.100115.
[5] Y. Chen, J. Wang, Z. Lv, J. Wang, F. Tian, L. Zhang, W. Zhang, H. Chen, M. Li, An innovative high-entropy alloy solder for high-reliability low-temperature bonding in 3D electronic packaging–based on nano InSnBiZnAg particles, J. Mater. Res. Technol. 30 (2024) 5622–5631, https://doi.org/10.1016/j.jmrt.2024.04.257.
[6] Y.-W. Lee, T.-K. Lee, J.-P. Jung, Intermediate low-melting-temperature solder thermal cycling enhancement using bismuth and indium microalloying, J. Electron. Mater. 52 (2023) 810–818, https://doi.org/10.1007/s11664-022-10121-y.
[7] D.L. Han, H. Tatsumi, F. Huo, H. Nishikawa, Effect of isothermal aging on properties of In-48Sn and In-Sn-8Cu alloys, in: 2022 IEEE 72nd Electronic Components and Technology Conference (ECTC), 2022, pp. 2148–2152, https://doi.org/10.1109/ECTC51906.2022.00339.
[8] X. Li, H. Andersson, J. Sidén, T. Schön, Soldering surface mount components on screen-printed Ag patterns on paper and polyimide substrates for hybrid printed electronics, Flex. Print. Electron. 3 (2018) 015003, https://doi.org/10.1088/2058-8585/aa9dc7.
[9] T. Aizawa, K. Okagawa, M. Kashani, Application of magnetic pulse welding technique for flexible printed circuit boards (FPCB) lap joints, J. Mater. Process. Technol. 213 (2013) 1095–1102, https://doi.org/10.1016/j.jmatprotec.2012.12.004.
[10] M. Layani, S. Magdassi, Flexible transparent conductive coatings by combining self-assembly with sintering of silver nanoparticles performed at room temperature, J. Mater. Chem. 21 (2011) 15378–15382, https://doi.org/10.1039/C1JM13174E.
[11] V. Zardetto, T.M. Brown, A. Reale, A. Di Carlo, Substrates for flexible electronics: a practical investigation on the electrical, film flexibility, optical, temperature, and solvent resistance properties, J. Polym. Sci. B 49 (2011) 638–648, https://doi.org/10.1002/polb.22227.
[12] L. Sun, L. Zhang, Properties and microstructures of Sn-Ag-Cu-X lead-free solder joints in electronic packaging, Adv. Mater. Sci. Eng. 2015 (2015) e639028, https://doi.org/10.1155/2015/639028.
[13] Y. Zhang, Z. Cai, J.C. Suhling, P. Lall, M.J. Bozack, The effects of aging temperature on SAC solder joint material behavior and reliability, in: 2008 58th Electronic Components and Technology Conference, 2008, pp. 99–112, https://doi.org/10.1109/ECTC.2008.4549956.
[14] G. Wu, J. Shen, D. Zhou, M. Khairi Faiz, Y.H. Wong, Applications and recent advances of low-temperature multicomponent solders in electronic packaging: a review, Micromachines 16 (2025) 300, https://doi.org/10.3390/mi16030300.
[15] JISZ3282:2017 はんだ−化学成分及び形状, (n.d.). https://kikakurui.com/z3/Z3282-2017-01.html (accessed March 30, 2023).
[16] D.L. Han, Y.-A. Shen, S. Jin, H. Nishikawa, Microstructure and mechanical properties of the In–48Sn–xAg low-temperature alloy, J. Mater. Sci. 55 (2020) 10824–10832, https://doi.org/10.1007/s10853-020-04691-7.
[17] F. Wang, M. O'Keefe, B. Brinkmeyer, Microstructural evolution and tensile properties of Sn–Ag–Cu mixed with Sn–Pb solder alloys, J. Alloys Compd. 477 (2009) 267–273, https://doi.org/10.1016/j.jallcom.2008.10.141.
[18] S.H. Rajendran, S.J. Hwang, J.P. Jung, Shear strength and aging characteristics of Sn-3.0Ag-0.5Cu/Cu solder joint reinforced with ZrO2 nanoparticles, Metals 10 (2020) 1295, https://doi.org/10.3390/met10101295.
[19] W. Zhu, W. Zhang, W. Zhou, P. Wu, Improved microstructure and mechanical properties for SnBi solder alloy by addition of Cr powders, J. Alloys Compd. 789 (2019) 805–813, https://doi.org/10.1016/j.jallcom.2019.03.027.
[20] W. Xing, X. Yu, H. Li, L. Ma, W. Zuo, P. Dong, W. Wang, M. Ding, Microstructure and mechanical properties of Sn-9Zn-xAl2O3 nanoparticles (x=0–1) lead-free solder alloy: first-principles calculation and experimental research, Mater. Sci. Eng. 678 (2016) 252–259, https://doi.org/10.1016/j.msea.2016.10.006.
[21] F. Huo, Z. Jin, D.L. Han, J. Li, K. Zhang, H. Nishikawa, Novel interface regulation of Sn1.0Ag0.5Cu composite solders reinforced with modified ZrO2: microstructure and mechanical properties, J. Mater. Sci. Technol. 125 (2022) 157–170, https://doi.org/10.1016/j.jmst.2022.01.040.

[22] S. Nitta, H. Tatsumi, H. Nishikawa, Strength-enhanced Sn–In low-temperature alloy with surface-modified ZrO2 nanoparticle addition, J. Mater. Sci. 34 (2023) 2066, https://doi.org/10.1007/s10854-023-11344-3.
[23] F. Huo, Y.-A. Shen, S. He, K. Zhang, H. Nishikawa, Fabrication of NiO/ZrO2 nanocomposites using ball milling-pyrolysis method, Vacuum 191 (2021) 110370, https://doi.org/10.1016/j.vacuum.2021.110370.
[24] V. Shepelevich, J. Wang, Structure and microhardness of rapidly solidified In-Sn foils, Inorg. Mater. 48 (2012), https://doi.org/10.1134/S0020168512050184.
[25] Y. Hirata, C. Yang, S. Lin, H. Nishikawa, Improvements in mechanical properties of Sn–Bi alloys with addition of Zn and In, Mater. Sci. Eng. 813 (2021) 141131, https://doi.org/10.1016/j.msea.2021.141131.
[26] P. Hohenberg, W. Kohn, Inhomogeneous electron gas, Phys. Rev. 136 (1964) B864–B871, https://doi.org/10.1103/PhysRev.136.B864.
[27] W. Kohn, L.J. Sham, Self-consistent equations including exchange and correlation effects, Phys. Rev. 140 (1965) A1133–A1138, https://doi.org/10.1103/PhysRev.140.A1133.
[28] OpenMX website, (n.d.). https://openmx-square.org/(accessed June 11, 2024).
[29] I. Morrison, D.M. Bylander, L. Kleinman, Nonlocal Hermitian norm-conserving Vanderbilt pseudopotential, Phys. Rev. B 47 (1993) 6728–6731, https://doi.org/10.1103/PhysRevB.47.6728.
[30] J.P. Perdew, K. Burke, M. Ernzerhof, Generalized gradient approximation made simple, Phys. Rev. Lett. 77 (1996) 3865–3868, https://doi.org/10.1103/PhysRevLett.77.3865.
[31] T. Ozaki, Variationally optimized atomic orbitals for large-scale electronic structures, Phys. Rev. B 67 (2003) 155108, https://doi.org/10.1103/PhysRevB.67.155108.
[32] T. Ozaki, H. Kino, Numerical atomic basis orbitals from H to Kr, Phys. Rev. B 69 (2004) 195113, https://doi.org/10.1103/PhysRevB.69.195113.
[33] D.R. Hamann, Optimized norm-conserving Vanderbilt pseudopotentials, Phys. Rev. B 88 (2013) 085117, https://doi.org/10.1103/PhysRevB.88.085117.
[34] K. Lejaeghere, G. Bihlmayer, T. Björkman, P. Blaha, S. Blügel, V. Blum, D. Caliste, I. E. Castelli, S.J. Clark, A. Dal Corso, S. de Gironcoli, T. Deutsch, J.K. Dewhurst, I. Di Marco, C. Draxl, M. Dułak, O. Eriksson, J.A. Flores-Livas, K.F. Garrity, L. Genovese, P. Giannozzi, M. Giantomassi, S. Goedecker, X. Gonze, O. Grånäs, E.K.U. Gross, A. Gulans, F. Gygi, D.R. Hamann, P.J. Hasnip, N.A.W. Holzwarth, D. Iuşan, D. B. Jochym, F. Jollet, D. Jones, G. Kresse, K. Koepernik, E. Küçükbenli, Y. O. Kvashnin, I.L.M. Locht, S. Lubeck, M. Marsman, N. Marzari, U. Nitzsche, L. Nordström, T. Ozaki, L. Paulatto, C.J. Pickard, W. Poelmans, M.I.J. Probert, K. Refson, M. Richter, G.-M. Rignanese, S. Saha, M. Scheffler, M. Schlipf, K. Schwarz, S. Sharma, F. Tavazza, P. Thunström, A. Tkatchenko, M. Torrent, D. Vanderbilt, M.J. van Setten, V. Van Speybroeck, J.M. Wills, J.R. Yates, G.-X. Zhang, S. Cottenier, Reproducibility in density functional theory calculations of solids, Science 351 (2016) aad3000, https://doi.org/10.1126/science.aad3000.
[35] K. Lejaeghere, V. Van Speybroeck, G. Van Oost, S. Cottenier, Error estimates for solid-state density-functional theory predictions: an overview by means of the ground-State elemental crystals, Crit. Rev. Solid State Mater. Sci. 39 (2014) 1–24, https://doi.org/10.1080/10408436.2013.772503.
[36] A.M. Ito, A. Takayama, O. Watanabe, V. Singh, S. Tyagi, S.S. Singh, Tuning of density functional theory simulation on vector processor system - plasma simulator Raijin -, Plasma Fusion Res. 15 (2020) 1203085, https://doi.org/10.1585/pfr.15.1203085. –1203085.
[37] C.J. Howard, R.J. Hill, The polymorphs of zirconia: phase abundance and crystal structure by Rietveld analysis of neutron and X-ray diffraction data, J. Mater. Sci. 26 (1991) 127–134, https://doi.org/10.1007/BF00576042.
[38] Z. Feng, V.S. Babu, J. Zhao, M.S. Seehra, Effect of magnetic dilution on magnetic ordering in NipMg1−pO, J. Appl. Phys. 70 (1991) 6161–6163, https://doi.org/10.1063/1.350030.
[39] T. Yang, X. Chen, W. Li, X. Han, P. Liu, First-principles calculations to investigate the interfacial energy and electronic properties of Mg/AlN interface, J. Phys. Chem. Solids 167 (2022) 110705, https://doi.org/10.1016/j.jpcs.2022.110705.
[40] F. Schwabl, Equilibrium ensembles, Ed, in: F. Schwabl (Ed.), Statistical Mechanics, Springer, Berlin, Heidelberg, 2006, pp. 25–74, https://doi.org/10.1007/3-540-36217-7_2.
[41] G. Navascues, Liquid surfaces: theory of surface tension, Rep. Prog. Phys. 42 (1979) 1131, https://doi.org/10.1088/0034-4885/42/7/002.
[42] S. Amares, R. Durairaj, S.H. Kuan, Experimental study on the melting temperature, microstructural and improved mechanical properties of Sn58Bi/Cu solder alloy reinforced with 1%, 2% and 3% zirconia (ZrO2) nanoparticles, Arch. Metall. Mater. (2021) 407–418, https://doi.org/10.24425/amm.2021.135872.
[43] W. Xing, X. Yu, H. Li, L. Ma, W. Zuo, P. Dong, W. Wang, M. Ding, Effect of nano Al2O3 additions on the interfacial behavior and mechanical properties of eutectic Sn-9Zn solder on low temperature wetting and soldering of 6061 aluminum alloys, J. Alloys Compd. 695 (2017) 574–582, https://doi.org/10.1016/j.jallcom.2016.11.136.
[44] H. Yang, Y. Huang, B. Song, K.U. Kainer, H. Dieringa, Enhancing the creep resistance of AlN/Al nanoparticles reinforced Mg-2.85Nd-0.92Gd-0.41Zr-0.29Zn alloy by a high shear dispersion technique, Mater. Sci. Eng. 755 (2019) 18–27, https://doi.org/10.1016/j.msea.2019.03.131.
[45] L.-Y. Chen, J.-Q. Xu, H. Choi, M. Pozuelo, X. Ma, S. Bhowmick, J.-M. Yang, S. Mathaudhu, X.-C. Li, Processing and properties of magnesium containing a dense uniform dispersion of nanoparticles, Nature 528 (2015) 539–543, https://doi.org/10.1038/nature16445.
[46] D. Luo, Y. Xiao, L. Wang, L. Liu, X. Zeng, M. Li, Interfacial reaction behavior and bonding mechanism between liquid Sn and ZrO2 ceramic exposed in ultrasonic waves, Ceram. Int. 43 (2017) 7531–7536, https://doi.org/10.1016/j.ceramint.2017.03.042.
[47] C. Hübsch, P. Dellinger, H.J. Maier, F. Stemme, M. Bruns, M. Stiesch, L. Borchers, Protection of yttria-stabilized zirconia for dental applications by oxidic PVD coating, Acta Biomater. 11 (2015) 488–493, https://doi.org/10.1016/j.actbio.2014.09.042.
[48] H. Ma, Z. Liu, L. Wu, Y. Wang, X. Wang, Study of a pre-treatment process for electroless copper plating on ceramics, Thin Solid Films 519 (2011) 7860–7863, https://doi.org/10.1016/j.tsf.2011.05.005.
[49] N. Eustathopoulos, B. Drevet, Determination of the nature of metal–oxide interfacial interactions from sessile drop data, Mater. Sci. Eng. 249 (1998) 176–183, https://doi.org/10.1016/S0921-5093(98)00521-8.
[50] Q. Lin, C. Ye, R. Sui, Wetting of Ni-based amorphous and crystalline alloys by Sn and Sn-based solders, Microelectron. Reliab. 111 (2020) 113722, https://doi.org/10.1016/j.microrel.2020.113722.
[51] C. Aparicio, Y. Maazouz, D. Yang, Measuring wettability of biosurfaces at the microscale, Eds, in: M. Navarro, J.A. Planell (Eds.), Nanotechnology in Regenerative Medicine: Methods and Protocols, Humana Press, Totowa, NJ, 2012, pp. 163–177, https://doi.org/10.1007/978-1-61779-388-2_11.
[52] R.P. Sear, Nucleation: theory and applications to protein solutions and colloidal suspensions, J. Phys. 19 (2007) 033101, https://doi.org/10.1088/0953-8984/19/3/033101.
[53] H. Yinnon, D.R. Uhlmann, A kinetic treatment of glass formation V: surface and bulk heterogeneous nucleation, J. Non-Cryst. Solids 44 (1981) 37–55, https://doi.org/10.1016/0022-3093(81)90131-9.
[54] T. Sugimoto, F. Shiba, A new approach to interfacial energy. 3. Formulation of the absolute value of the solid−liquid interfacial energy and experimental collation to silver halide systems, J. Phys. Chem. B 103 (1999) 3607–3615, https://doi.org/10.1021/jp984348g.
[55] T. Phongpreecha, J.D. Nicholas, T.R. Bieler, Y. Qi, Computational design of metal oxides to enhance the wetting and adhesion of silver-based brazes on yttria-stabilized-zirconia, Acta Mater. 152 (2018) 229–238, https://doi.org/10.1016/j.actamat.2018.04.024.
[56] G. Dey, J. Ren, T. El-Ghazawi, S. Licht, How does an amalgamated Ni cathode affect carbon nanotube growth? A density functional theory study, RSC Adv. 6 (2016) 27191–27196, https://doi.org/10.1039/C6RA03460H.
[57] N. Eustathopoulos, M.G. Nicholas, B. Drevet, Wettability At High Temperatures, Elsevier, 1999.
[58] G.C. Sosso, J. Chen, S.J. Cox, M. Fitzner, P. Pedevilla, A. Zen, A. Michaelides, Crystal nucleation in liquids: open questions and future challenges in molecular dynamics simulations, Chem. Rev. 116 (2016) 7078–7116, https://doi.org/10.1021/acs.chemrev.5b00744.